LASER & PHOTONICS REVIEWS
www.lpr-journal.org

Composition-Graded Perovskite Microwire Toward Broad Wavelength Tunable Single-Mode Lasing

Junfeng Lu, Xiaopeng He, Fangtao Li, Meili Li, Sihao Xia, Linglong Zhang, Xiaoxuan Wang, Juan Xu, Yizhi Zhu, Chaoyang Huang, Yanda Ji, Caixia Kan, Chunxiang Xu,* and Caofeng Pan**

Continuously manipulating the resonant wavelength of lasing modes within a large spectral range is of great significance for expanding device functionality. Here, to synthesize a single $CsPbCl_xBr_{3-x}$ perovskite microwire with the energy bandgap gradient spanning from 2.33 to 2.83 eV along the length direction defined as the axis by using the vapor-phase anion exchange method is proposed. A high-quality (≈10^3), wide range (≈60 nm), and continuously tunable single-mode laser is achieved in as-prepared perovskite microwire alloy, which provides both gain media and microresonator. Simultaneously, the exciton recombination dynamics and atomic-scale interdiffusion mechanisms at different components are clarified through time-resolved photoluminescence (PL) spectra and theoretical calculations. The vacancy defects have a significant impact on the interdiffusion of halogen anions, excitonic recombination lifetime, and fluorescence quantum efficiency. The work provides a new strategy for the construction of new-type broadband tunable lasers and high-precision microspectrometers.

1. Introduction

A broadly and continuously tunable wavelength for semiconductor lasers is an important requirement in practical applications, which can provide a new-type multifunctional coherent light source for all-optical integrated chips and optical interconnection systems. In the past decade, a lot of efforts have been devoted to the research in tunable lasers, leading to the emergence of many manipulated methods, such as the self-absorption effect,[1,2] Burstein-Moss (BM) effect,[3,4] physical field,[5–12] bandgap engineering.[13–16] The most representative method in terms of broadband wavelength tunable capability is bandgap engineering, which has been achieved by controlling the compositions in many II-VI and III-V semiconductor materials.[17,18] Unfortunately, the fabrication of these semiconductor micro/nanostructures requires expensive high-temperature and low-pressure conditions. In addition, the spatially independent separation of several nanowire alloys with different emission wavelengths also hinders their integration with photonic and optoelectronic devices. Therefore, it is urgent to search for an ideal semiconductor gain medium with an easily fabricated method for constructing a single microcavity alloy with a gradient bandgap distribution.

Perovskite, as an emerging semiconductor material, has attracted extensive applications in optoelectronics such as light-emitting diodes,[19–21] lasers,[22–24] photodetectors,[25–27] and solar cells,[28–30] due to its high fluorescence quantum efficiency, widely tunable bandgap, high optical absorption coefficient, as well as solution-phase processability.[31] By adjusting the

J. Lu, X. He, S. Xia, L. Zhang, J. Xu, Y. Ji, C. Kan
College of Physics
Nanjing University of Aeronautics and Astronautics
Nanjing 211106, P. R. China
E-mail: lujunfeng@nuaa.edu.cn

J. Lu, X. He, S. Xia, L. Zhang, J. Xu, Y. Ji, C. Kan
Key Laboratory of Aerospace Information Materials and Physics (NUAA)
MIIT
Nanjing 211106, P. R. China

F. Li
School of Physics and Electronic Engineering
Xinyang Normal University
Xinyang 464000, P. R. China

M. Li, C. Pan
Institute of Atomic Manufacturing
Beihang University
Beijing 100191, P. R. China
E-mail: pancaofeng@buaa.edu.cn

M. Li, Y. Zhu
Beijing Institute of Nanoenergy and Nanosystems
Chinese Academy of Sciences
Beijing 100083, P. R. China

X. Wang, C. Huang, C. Xu
State Key Laboratory of Bioelectronics
School of Biological Science and Medical Engineering
Southeast University
Nanjing 210096, P. R. China
E-mail: xcxseu@seu.edu.cn

The ORCID identification number(s) for the author(s) of this article can be found under https://doi.org/10.1002/lpor.202400555

DOI: 10.1002/lpor.202400555

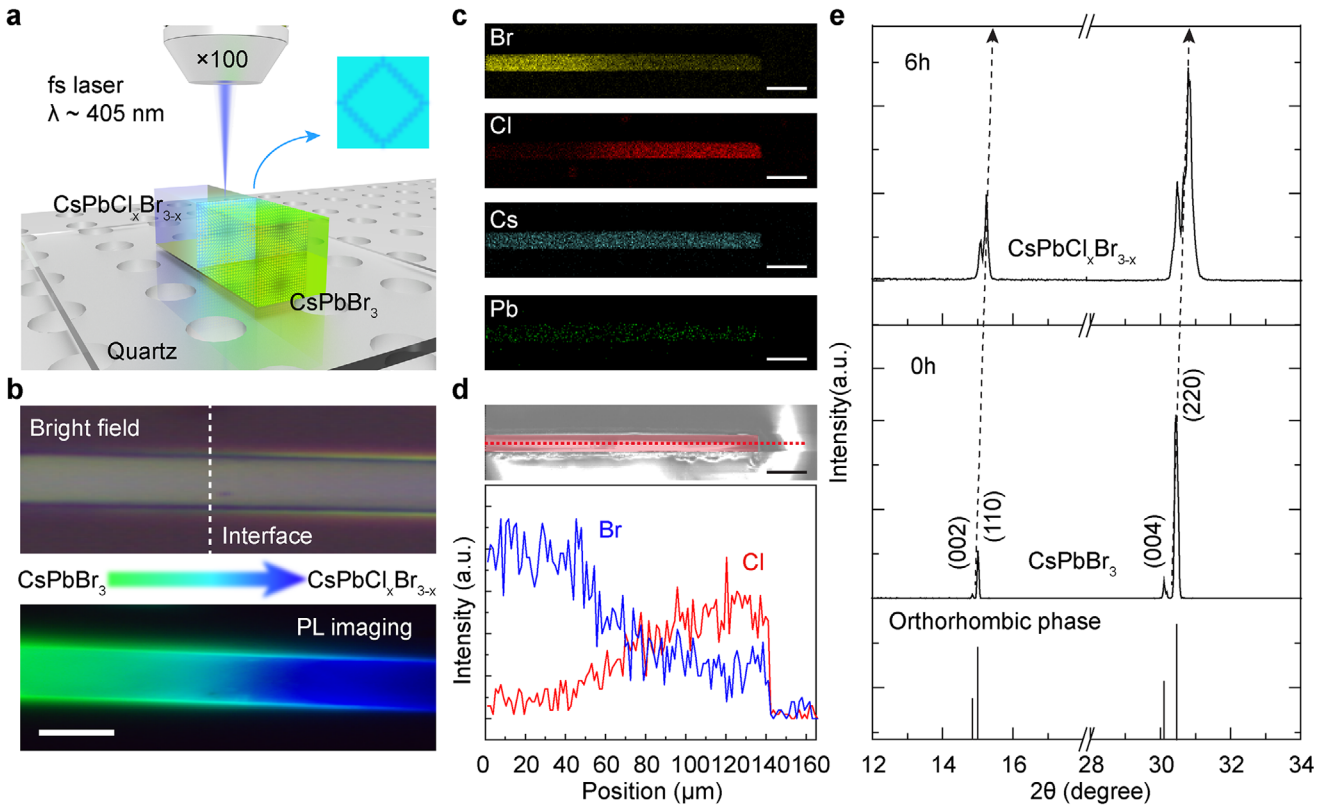

Figure 1. Morphology, structure, and elemental characterization. a) Schematic diagram of in-situ pumping for single perovskite microwire alloy with gradually changing halogen components along the axial direction. b) Bright-field optical images (up panel) and dark-field photoluminescence (PL) mapping (down panel) of the prepared single $CsPbBr_3$-$CsPbCl_xBr_{3-x}$ alloy microwire, scale bar: 10 μm. c) EDS element mapping of single perovskite alloy microwire, Yellow: bromine; Red: chlorine; Blue: cesium; Green: lead, scale bar: 20 μm. d) SEM image of the same sample and the corresponding chlorine (red line) and bromine (blue line) distribution profiles along the microwire axis, scale bar: 20 μm. e) XRD patterns of the as-grown $CsPbBr_3$ perovskite microwires and $CsPbCl_xBr_{3-x}$ perovskite microwires after halogen anion exchange lasting for 6 h.

composition of halogen elements in perovskite, broad tunability covering the near-infrared to visible wavelength region can be achieved, providing the possibility of modulating laser output frequency over a wide range.[32,33] Typically, Zhu and co-workers[34] realized broad wavelength tunability in perovskite alloy nanowires based on controllable halogen stoichiometry in the precursor solution. Also, the perovskite alloy with a gradient distribution of halogen components along the length direction can be realized on a single nanowire through anion exchange,[35–37] due to the low activation energy of halogen ion migration and soft lattice characteristics. Representatively, Jin and co-workers,[38] reported the gradient distributed bandgap on a single perovskite nanowire through the solid-phase anion exchange method with the photoluminescence (PL) wavelength covering from ≈485 to ≈525 nm, and investigating the anion interdiffusion kinetics processes systematically. This unique composition gradient configuration and regular geometric construction not only provides an ideal platform for exploring the intrinsic halide anion interdiffusion but also provides a promising route for designing the broadly and continuously wavelength-tunable lasers[39] and single-nanowire micro spectrometers.[40,41]

Herein, the gradient distribution of bandgap along the axis is realized successfully based on the gas-phase anion exchange in a single perovskite microwire which serves as both an optical gain medium and an optical resonator. The PL emission wavelength covering from ≈440 to ≈520 nm provides ongoing and reliable gain compensation for the widely and continuously tunable lasing output, as the excitation spot moves axially along the prepared microwire. Also, the exciton recombination dynamics in the diffusion region and the atomic-scale mechanism of anion interdiffusion have been systematically investigated through time-resolved PL measurement and first-principles calculations, which can be found that vacancies and their hopping play an important role in both physical processes. According to the ideal semi-infinite model and theoretical calculations, the diffusion coefficient is estimated to be 3.26×10^{-10} cm^{-2} s^{-1} at a reaction temperature of 190 °C, whereas the migration activation energies of bromine and chlorine along the <110> direction are 0.35 and 0.41 eV, respectively, indicating that the migration of the former is easier.

2. Results and Discussion

Figure 1a shows the schematic diagram of the in situ optical signal acquisition unit for a single perovskite microwave alloy with a halogen gradient changing along the axial direction. The focusing of excited light and the collection of emitted light are manipulated through the same objective lens, accompanied by a 3D

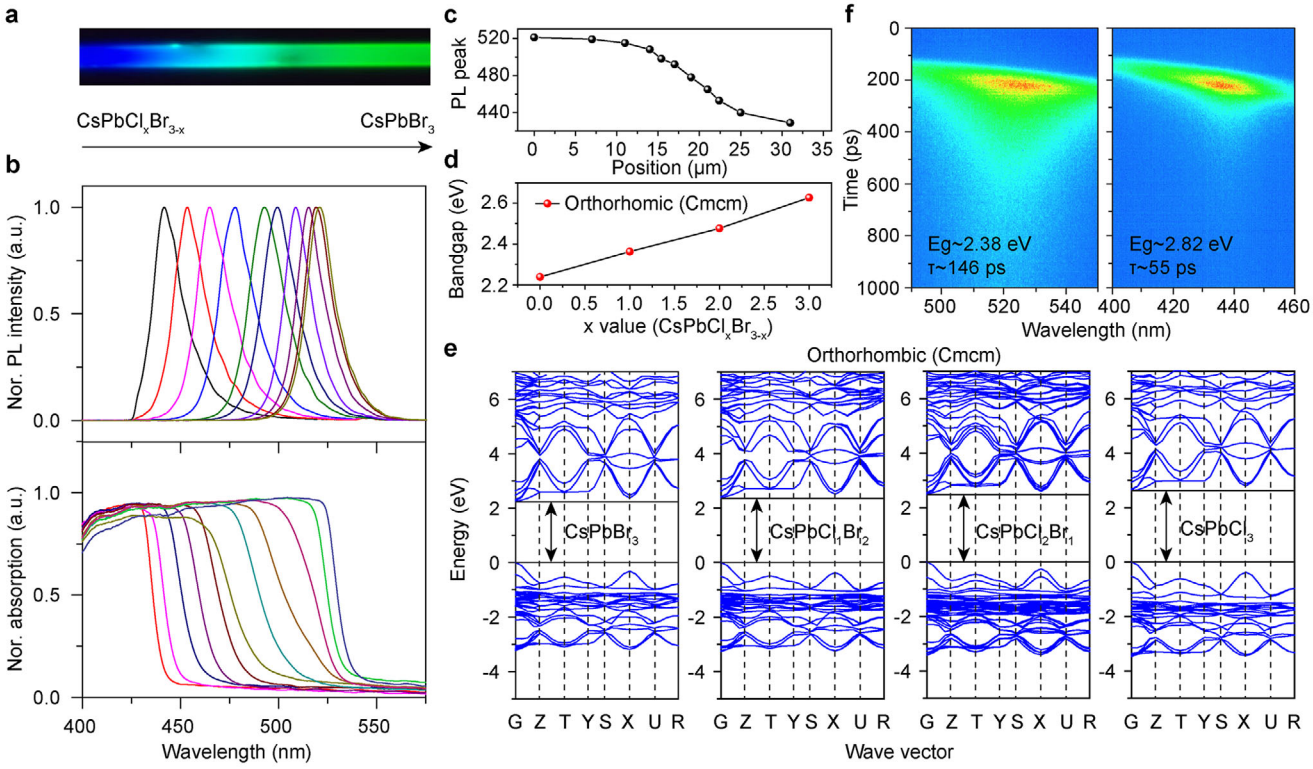

Figure 2. Optical performance and theoretical calculations. a) The real-color PL mapping of single CsPbCl$_x$Br$_{3-x}$ perovskite alloy microwire with gradient composition. b) PL (upper panel) and absorption (lower panel) spectra of this single CsPbCl$_x$Br$_{3-x}$ perovskite alloy microwire measured at different positions along the gradient direction. c) The dependence of PL peak wavelength on distance of the corresponding perovskite alloy microwire. d) The dependence of band gap on the x value of CsPbCl$_x$Br$_{3-x}$ perovskite alloy microwire. e) The electronic structures of four typical halogen components at different spots along the gradient direction. f) Temporal spectroscopic profiles of the CsPbCl$_x$Br$_{3-x}$ perovskite alloy microwire with an energy bandgap of ≈2.38 and ≈2.82 eV were collected by a streak camera.

displacement table to control the excitation position. Figure 1b demonstrates the optical images of bright- and dark-field PL imaging of a single perovskite microwire near the Cl ion exchange interface. The typical gradient from green emission to blue emission along the axis is observed, indicating the successful exchange of Cl ions. Meanwhile, the surface of the region exchanged by Cl ions remains smooth, providing a necessary prerequisite for high-quality lasing mode output. To further confirm the exchange of Cl ions, the energy dispersive X-ray spectroscopy (EDS) mapping of single perovskite microwire alloy with the halogen gradient along the axial direction is measured, as shown in Figure 1c. It can be observed that the bromine elements (yellow) and chlorine elements (red) exhibit a gradient change process near the exchange interface area, while other elements such as cesium (blue) and lead (green) are evenly distributed throughout the entire nanowire. The line scan profiles (red dotted line in upper panel) of bromine and chlorine shown in Figure 1d further illustrate that the concentration of these two elements is distributed in a gradient along the axis. To demonstrate the universality of the gas-phase anion exchange method, the structural evolution of perovskite nanowires before and after the exchange is described by the X-ray diffraction (XRD) pattern in Figure 1e. The two strong diffraction peaks of the as-grown $CsPbBr_3$ perovskite microwires are located at 15.01° and 30.45°, which can be well-assigned to the (110) and (220) lattice planes of the orthorhombic-phase perovskite-type $CsPbBr_3$ (space group *Pbnm*, a = 8.202 Å, b = 8.244 Å, c = 11.748 Å). The obvious splitting of the (002) and (110) diffraction peaks strongly suggests the distorted perovskite structure with tilted PbX_6 octahedra at room temperature. As the chloride ion exchange process lasts for 6 h, the (110) and (220) diffraction peaks of perovskite microwires shifted significantly from 15.01° and 30.45° to 15.26° and 30.80°. It implies that the exchange of chloride ions significantly reduces the interplanar spacing according to Bragg's law ($2d\sin\theta = n\lambda$) due to its relatively small ionic radius. The investigations mentioned above have confirmed that a single perovskite microwave alloy with a gradient distribution of halogen along the axial direction has been prepared via the gas-phase anion exchange method in success.

The perovskite nanowires exchanged by chloride ions along the axis exhibit a continuous color transition from blue to cyan, and then to green under the illumination of a 385 nm laser, as shown in real-color PL mapping of **Figure 2**a. PL spectra at the corresponding spots are measured through a homemade microscopy system equipped with a spectrometer and CCD, as shown in the upper panel of Figure 2b. It can be observed that the PL signals collected at each spot along the axis exhibit a strong single peak emission, indicating that the distribution of chloride ions at each excitation spot in the lattice is relatively uniform. Over the entire measurement span, the emission wavelength

coverage of PL spectra ranges from ≈440 to ≈520 nm as the excited spot moves from one end to the other. Figure 2c demonstrates the dependence of PL peak wavelengths on the excitation positions, suggesting the formation of the gradient-distributed bandgap along the axial direction. The micro-absorption spectra at different measured spots shown in the lower panel of Figure 2b further confirm that the energy bandgap of single perovskite microwire alloy is distributed in a gradient along the axial direction, spanning from 2.33 to 2.83 eV (see Figure S4 in the Supporting Information). Theoretically, the electronic structures of alloy microwire have been calculated based on density functional theory, as shown in Figure 2e. The investigation results show that the bandgap continuously broadens as the chloride ion content increases, which is consistent with the observed redshift phenomenon of PL emission wavelength in experiments. Figure 2d plots the dependence of the bandgap on chloride ion content (x value), showing a linear increasing tendency following Vegard's law. In order to systematically study the dynamics of perovskite microwire alloy with the gradient bandgap distributed along the axial direction, the measurement of time-resolved photoluminescence (TRPL) spectra is performed through the μ-PL system equipped with a streak camera, as shown in Figure 2f and Figure S5 (Supporting Information). Temporal spectroscopic profiles of the perovskite alloy microwire with energy bandgap ranging from ≈2.38 to ≈2.82 eV are collected, corresponding to the transition from the narrow-bandgap Br-rich region to the wide-bandgap Cl-rich region. The PL lifetime from the Cl-rich region to the Br-rich region is analyzed by the fitting of the single-exponential decay function, $y(t) = A_0 + A_1\exp(-t/\tau)$, where τ is the decay time. The Br-rich region exhibits a longer PL lifetime compared to the Cl-rich region, which is consistent with the variation tendencies reported before.[35,37] The dominant factor is the increase in vacancy defects in the lattice caused by the exchange of Cl ions, serving as nonradiative recombination centers with distinct local PL lifetimes. In comparison, the nonradiative recombination centers capture the excited electrons faster, resulting in a shorter PL lifetime at the Cl-rich end. On the other hand, more carriers are captured by nonradiative recombination centers rather than radiative recombination in the Cl-rich region, resulting in lower fluorescence quantum efficiency compared to the Br-rich region. This is also one of the reasons for the higher lasing threshold in the Cl-rich region, which will be discussed in detail later. To verify the reproducibility of the gas phase anion exchange method, two additional perovskite micron wire alloys with an axial gradient distribution of energy bands were prepared (see Figure S4 in the Supporting Information). The PL spectra at different excitation sites along the axial direction show that the method has good repeatability and operability.

In order to clarify the atomic scale interdiffusion mechanism of halogen anions, this method was implemented to discover possible transition states. **Figure 3**a systematically describes the whole process of halogen anion exchange, which can be divided into three parts: the $CsPbCl_3$ region, which provides Cl ions (represented by the black dashed box on the left); diffusion region, where the interdiffusion process mainly occurs; $CsPbBr_3$ region, where provides Br ions (represented by the black dashed box on the right). The red and black arrows in Figure 3b,c represent the migration paths of Br and Cl ions along the <100> direction, respectively. The energy profiles and typical transition states of Br ion and Cl ion migration along the <100> direction are demonstrated in Figure 3d, with the highest activation energies of 0.86 and 1.02 eV, respectively, indicating that the migration of Br ion is easier than that of Cl ion. Similarly, the red and black arrows in Figure 3e,f represent the migration paths of Br and Cl ions along the <110> direction, with the activation energies of 0.35 and 0.41 eV shown in Figure 3g, respectively. This also illustrates that the migration of Br ions along the <110> direction is easier than that of Cl ions, both of which are consistent with the previous reports.[37] Overall, the migration activation energy of the two halogen anions along the <100> direction is higher than that along the <110> direction, mainly due to the fact that the migration in the <100> direction across crystal cells breaks one more Pb-X (Br, Cl) bonds than the migration in the <110> direction within the same crystal cell. In this case, the interdiffusion process of halogen anions follows a vacancy-mediated mechanism, which was further confirmed in the experiment, as shown in Figure 3h. The thermal diffusion experiments at 190 °C are performed, in which the same as-prepared sample is annealed for different times of 4, 8, and 12 h, respectively. The PL emission wavelengths at the same relative positions before and after annealing are monitored, and it can be found that the interdiffusion length is ≈68 μm after continuous heating for 12 h. Also, it can be observed that the variation rate of emission wavelength in the Br-rich region is slower than that in the Cl-rich region as a whole, especially when the annealing time is not sufficient (annealing for 4 h). It indicates that the diffusion of Cl ions is more difficult than that of Br ions, which is consistent with the previous theoretical predictions and reports.[35] Figure 3i plots the dependence of diffusion length on the square root of reaction time, showing a linear relationship fitting by the function of $L \cong 2\sqrt{Dt}$ for an ideal semi-infinite model.[35,38] This dynamic behavior conforms to the diffusion theory involving a constant diffusion coefficient D, which can be estimated as 3.26×10^{-10} cm^{-2} s^{-1} by the linear fitting slope at the annealing temperature of 190 °C, which is consistent with previous reports.[38] The theoretical calculation and experimental results at the atomic scale manifest that the lower diffusion barriers of bromine and chloride ions contribute to their migration and interdiffusion processes, and effectively promote the formation of the perovskite alloy microwire with energy bandgap gradient distribution along the axial direction.

Single perovskite alloy microwire with energy bandgap gradient distribution along the axial direction is a natural resonator and gain media for building the new-type laser with broadly and continuously tunable wavelength. The lasing performances of single $CsPbCl_xBr_{3-x}$ alloy microwire shown in **Figure 4** are characterized by a confocal μ-PL system equipped with a 405 nm femtosecond pulse laser (190 fs, 6 KHz) and a 1200 g mm^{-1} optical multichannel spectrometer. Figure 4a shows the 2D pseudo-color lasing spectra in the Br-rich region under different pumping energy fluences with the resonant wavelength of the dominant lasing peak located at 534 nm. At lower energy fluence, a wide weak spontaneous emission peak located at 525.4 nm can be observed with the full width at half maximum (FWHM) of ≈25 nm. As the energy fluence increases gradually, some discrete peaks appear and rapidly increase, accompanied by a dramatic decrease

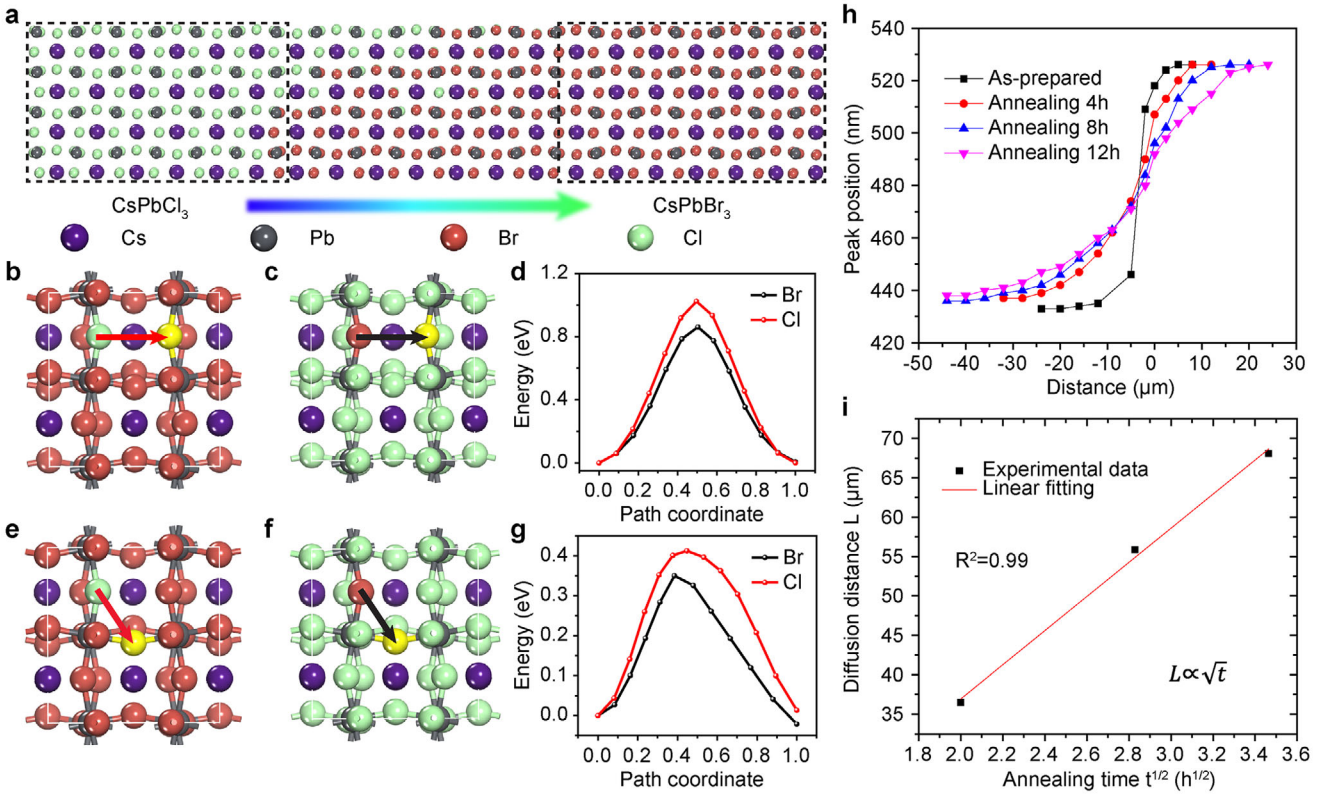

Figure 3. Halogen anions interdiffusion process and diffusion distance. a) An overall schematic of the anionic interdiffusion process between $CsPbBr_3$ and $CsPbCl_3$ perovskite. Schematic diagram of inter-cell migration for b) Cl ion (red arrow) and c) Br ion (black arrow). d) The corresponding energy profiles of different locations in the Cl ion and Br ion migration path. Schematic diagram of intra-cell migration for e) Cl ion (red arrow) and f) Br ion (black arrow). g) The corresponding energy profiles of different locations in the Cl ion and Br ion migration path. h) PL peak positions as a function of distance for the as-prepared and annealed gradient component perovskite alloy microwires with different annealing times at 190 °C. (i) The dependence of plot and linear fitting for diffusion length on the square root of reaction time ($t^{1/2}$).

in FWHM to 0.12 nm. It suggests a transition from spontaneous emission to stimulated emission with a lasing threshold of 0.43 mJ cm^{-2} shown in Figure 4c, which is clearly observed in the 2D pseudo-color plot of lasing spectra. Also, the rapid decay with a lifetime of 23.67 ps forms when the pumping energy density exceeds the lasing threshold, further implying the occurrence of an effective stimulated emission process (see Figure S7 in the Supporting Information). In this case, a single perovskite microwire with a tetragonal cross-section is a natural whispering-gallery microcavity (WGM), providing the configuration for total internal reflection and propagation of light waves at the inner walls. Combined with the plane-wave model and steady-state oscillation condition of laser, the expression of mode number for tetragonal whispering-gallery microcavity can be derived as $N = \frac{2\sqrt{2}nL}{\lambda} - \frac{4}{\pi}tan^{-1}(\beta\sqrt{n^2-2})$, where λ is the wavelength, n is the refractive index, L is the length of the cavity. The mode spacing can be described by the equation of $\delta\lambda = \frac{\lambda^2}{2\sqrt{2}Ln_g}$ The group refractive index can be extracted to ≈4.0 for the different sized perovskite microwires (see Figure S8 in the Supporting Information), which is consistent with previous reports,[42] suggesting the formation of square whispering-gallery mode lasing. Meanwhile, the formula of $Q = \lambda/\Delta\lambda$ is used to estimate the lasing quality (Q) factor in the Br-rich region, which is ≈4800 (see Figure S9 in the Supporting Information), indicating the effective optical-field confinement and low energy loss in as-prepared perovskite microwire. As the excited spot moves along the axial direction toward Cl-rich regions, the resonant wavelength of the lasing mode will shift blue gradually. Figure 4b shows 2D pseudo-color lasing spectra at different pumping energy fluences in the exchange region with the lasing wavelength of 495 nm. The dependence of integrated lasing intensity and FWHM on energy fluences demonstrates a similar tendency with that in the Br-rich region shown in Figure 4d, as the pumping energy fluences exceed the lasing threshold of 0.96 mJ cm^{-2}. The increase in the lasing threshold indicates a decrease in optical gain, due to an increase in nonradiative recombination centers and a decrease in fluorescence quantum efficiency induced by the diffusion of Cl ions, as mentioned before. In addition, the decrease in lasing quality further confirms that the introduction of vacancy defects weakens the confinement ability of the optical field for the microcavity, but it remains above the third order of magnitude (≈2400). Figure 4e shows the lasing spectra of single $CsPbCl_xBr_{3-x}$ perovskite microwire alloy recorded at different excited spots along the axis, with a tunable resonant wavelength ranging from 475 to 542 nm, covering ≈60 nm. The electric-field distribution of the fundamental modes at different

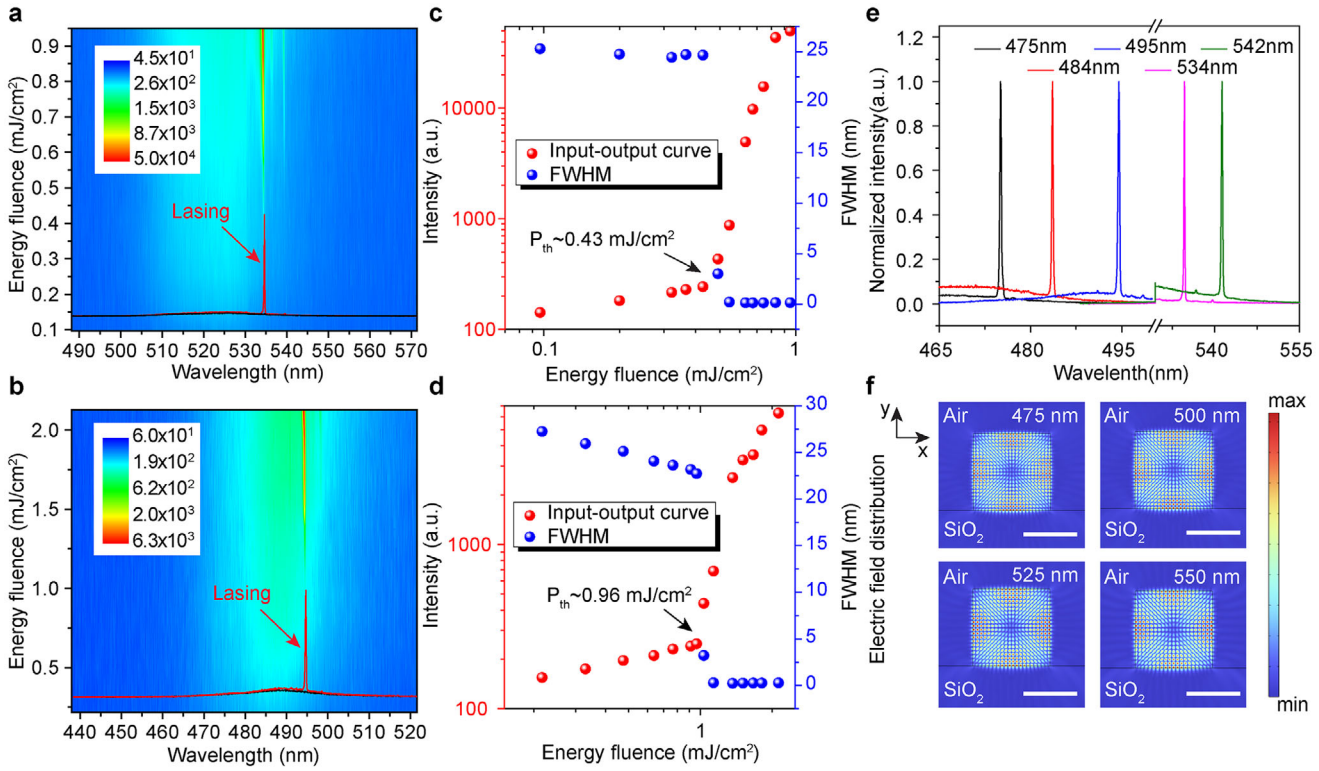

Figure 4. A broadly and continuously wavelength-tunable lasing mode output in single gradient component perovskite alloy microwire. 2D color plots of lasing spectra with the central wavelengths of 534 nm a) and 495 nm b) at different energy fluence. The dependence of the integrated lasing intensity and FWHM on energy fluence for the corresponding central wavelengths of 534 nm c) and 495 nm d), indicates the threshold behavior. e) The lasing spectra collected at different locations along the single perovskite alloy microwire with gradient components, showing the tunable wavelengths of 475 nm, 484 nm, 495 nm, 534 nm, and 542 nm, respectively. f) The electric-field distribution of the fundamental mode with different resonant wavelengths at 475, 500, 525, and 550 nm in the *x*-*y* plane, scale bar: 2 μm.

resonant wavelengths of 475, 500, 525, and 550 nm was also simulated using the FDTD method, as shown in Figure 4f, indicating the formation of typical tetragonal whispering-gallery oscillation modes. These results fully certify the ability of single perovskite microwire alloy with halogen gradient distribution along the axis to construct high-quality, broad-range, and continuously tunable lasers.

3. Conclusion

To summarize, a single $CsPbCl_xBr_{3-x}$ perovskite microwire alloy with gradient distributed bandgap along the axial direction is constructed in success by the anion gas exchange method with the PL spectral range covering from ≈440 to ≈520 nm. This new type of alloy microcavity enables us to investigate the single-mode WGM lasers with continuous and wide-range tunable wavelength when the excited spot moves along the axis. In comparison, the lower migration activation energy of Br ions and diffusion along the <110> direction is observed, which also be confirmed by experimental results and theoretical calculations through density functional theory (DFT). These results not only provide the reliable configuration for building high-quality, wide spectral range, continuously tunable laser but also profoundly clarify the atomic scale mechanism of halogen anion interdiffusion and the dynamics of exciton recombination.

4. Experimental Section

Preparation of Single $CsPbCl_xBr_{3-x}$ Perovskite Alloy Microwire: Single $CsPbBr_3$ perovskite microwire prepared using an anti-solvent method consistent with previous reports[2,5] (see Figure S1 and S2 in the Supporting Information) is selected and transferred to a 2 × 2 cm^2 glass slide through a home-made micromanipulation system. Then, a part of a single $CsPbBr_3$ perovskite microwire is covered with heat release tape and placed in a glass culture dish with a diameter of 13 mm and height of 2.5 mm containing 20 g anhydrous calcium chloride as a desiccant. Subsequently, 40 μL of 37 wt.% hydrochloric acid is absorbed by using a pipette whose thick end is sealed and put into the culture dish. The culture dish was encapsulated and placed in a 65 °C drying oven for a reaction time of 7 h. Later, the sample was taken out and placed on a 130 °C heating table for 30 s to remove the heat release tape and diffuse. Finally, the as-prepared single $CsPbCl_xBr_{3-x}$ perovskite alloy microwire is obtained (see Figure S3 in the Supporting Information).

Morphological, Structural, and Optical Characteristics: The morphology and composition analysis of single $CsPbCl_xBr_{3-x}$ perovskite alloy microwire is characterized by a field emission scanning electron microscope (FESEM, Hitachi SU8020) equipped with X-ray energy dispersion spectroscopy (EDS, LRXF Systems). The structural properties are characterized by X-ray diffraction (XRD, Panalytical Empyrean). The PL and absorption spectra and fluorescence imaging were measured by a highly integrated homemade microscopy system. The measurement of lasing characteristics is performed by a confocal μ-PL system, consisting of a femtosecond pulse laser (pulse width ≈190 fs, repetition frequency ≈6 KHz) with a wavelength of 405 nm, an upright microscope equipped with a

100× objective and Nikon camera, and an optical multi-channel spectrometer (Andor, SR-500i-D1-R) with a grating of 1200 g mm^{-1}. TRPL spectra are collected by a streak camera (Optronics, SC-10) with a resolution of 2 ps.

Theoretical Calculations: The first principle calculations are performed within CASTEP module based on density functional theory. The exchange and correlation interactions are processed by the generalized gradient approximation (GGA). The ionic core is described by OTFG ultrasoft pseudopotential. The valence electrons are addressed by Cs: 5s25p66s1, Pb: 5s25p65d106s26p2, Br: 4s24p5, and Cl: 3s23p5. Both HSE06 and PBE functionals are utilized with respect to the calculation of band structures. The cutoff energy and k-mesh point for PBE functional are respectively set as 320 eV and $6 \times 6 \times 4$ while that for HSE06 is 820 eV and $8 \times 8 \times 6$. The parameters of ground-state energy convergence in geometry optimization are set as 1×10^{-5} eV $atom^{-1}$ of energy, 0.03 eV $Å^{-1}$ of maximum force, 0.001 Å of maximum displacement, and 0.05 GPa of maximum stress. The diffusion barrier of Br and Cl is calculated by the energy difference between the total energy of the transition state and the initial ground state. The generalized synchronous transit method (LST/QST) is used for the discovery of a possible transition state, which is further confirmed by the conjugate gradient (CG) minimization.

Numerical Simulations: The electric-field distributions of the resonant modes with different wavelengths are simulated by the finite element method (finite-difference time-domain solution, FDTD). The excitation wavelength is set as 405 nm, and the monitoring wavelengths are 475, 500, 525, and 550 nm, respectively. The size and refractive index of the resonant microcavity are set as 3 μm and 2.54 respectively, and the refractive index of the SiO_2 substrate is set as 1.45.

Supporting Information

Supporting Information is available from the Wiley Online Library or from the author.

Acknowledgements

J.F.L., X.P.H., F.T.L., and M.L.L. contributed equally to this work. The authors thank the support of the Natural Science Foundation of Jiangsu Province (Grant No. BK20231441), the Fundamental Research Funds for the Central Universities (Grant No. NS2024063), National Natural Science Foundation of China (Grant Nos. 61805015, 62105035), Postgraduate Research and Practice Innovation Project of Nanjing University of Aeronautics and Astronautics (Grant No. xcxjh20222101).

Conflict of Interest

The authors declare no conflict of interest.

Data Availability Statement

The data that support the findings of this study are available from the corresponding author upon reasonable request.

Keywords

anion exchange, bandgap engineering, laser, perovskite, tunable wavelength

Received: April 19, 2024
Revised: July 3, 2024
Published online:

[1] Q. Zhang, S. T. Ha, X. Liu, T. C. Sum, Q. Xiong, *Nano Lett.* **2014**, *14*, 5995.
[2] J. Lu, C. Zhang, F. Li, R. Wang, F. Qin, G. Zhu, *Appl. Phys. Lett.* **2022**, *120*, 171105.
[3] X. Liu, Q. Zhang, J. N. Yip, Q. Xiong, T. C. Sum, *Nano Lett.* **2013**, *13*, 5336.
[4] J. S. Manser, P. V. Kamat, *Nat. Photonics* **2014**, *8*, 737.
[5] A. Guarino, G. Poberaj, D. Rezzonico, R. Degl'Innocenti, P. Günter, *Nat. Photonics* **2007**, *1*, 407.
[6] M. Humar, M. Ravnik, S. Pajk, I. Muševič, *Nat. Photonics* **2009**, *3*, 595.
[7] M. Mur, J. A. Sofi, I. Kvasić, A. Mertelj, D. Lisjak, V. Niranjan, I. Muševič, S. Dhara, *Opt. Express* **2017**, *25*, 1073.
[8] J. Lu, C. Xu, F. Li, Z. Yang, Y. Peng, X. Li, M. Que, C. Pan, Z. L. Wang, *ACS Nano* **2018**, *12*, 11899.
[9] Z. Yang, J. Lu, M. ZhuGe, Y. Cheng, J. Hu, F. Li, S. Qiao, Y. Zhang, G. Hu, Q. Yang, D. Peng, K. Liu, C. Pan, *Adv. Mater.* **2019**, *31*, 1900647.
[10] Y. Ueda, T. Shindo, S. Kanazawa, N. Fujiwara, M. Ishikawa, *Optica* **2020**, *7*, 1003.
[11] C. Wang, R. Ma, D. Peng, X. Liu, J. Li, B. Jin, A. Shan, Y. Fu, L. Dong, W. Gao, Z. L. Wang, C. Pan, *InfoMat* **2021**, *3*, 1272.
[12] Q. Zhang, S. Zuo, P. Chen, C. Pan, *InfoMat* **2021**, *3*, 987.
[13] A. Pan, W. Zhou, E. S. P. Leong, R. Liu, A. H. Chin, B. Zou, C. Z. Ning, *Nano Lett.* **2009**, *9*, 784.
[14] Y.-J. Lu, C.-Y. Wang, J. Kim, H.-Y. Chen, M.-Y. Lu, Y.-C. Chen, W.-H. Chang, L.-J. Chen, M. I. Stockman, C.-K. Shih, S. Gwo, *Nano Lett.* **2014**, *14*, 4381.
[15] G. Xing, N. Mathews, S. S. Lim, N. Yantara, X. Liu, D. Sabba, M. Grätzel, S. Mhaisalkar, T. C. Sum, *Nat. Mater.* **2014**, *13*, 476.
[16] J. Song, J. Li, X. Li, L. Xu, Y. Dong, H. Zeng, *Adv. Mater.* **2015**, *27*, 7162.
[17] F. Qian, Y. Li, S. Gradečak, H.-G. Park, Y. Dong, Y. Ding, Z. L. Wang, C. M. Lieber, *Nat. Mater.* **2008**, *7*, 701.
[18] Z. Yang, D. Wang, C. Meng, Z. Wu, Y. Wang, Y. Ma, L. Dai, X. Liu, T. Hasan, X. Liu, Q. Yang, *Nano Lett.* **2014**, *14*, 3153.
[19] Z.-K. Tan, R. S. Moghaddam, M. L. Lai, P. Docampo, R. Higler, F. Deschler, M. Price, A. Sadhanala, L. M. Pazos, D. Credgington, F. Hanusch, T. Bein, H. J. Snaith, R. H. Friend, *Nat. Nanotechnol.* **2014**, *9*, 687.
[20] Y. Cao, N. Wang, H. Tian, J. Guo, Y. Wei, H. Chen, Y. Miao, W. Zou, K. Pan, Y. He, H. Cao, Y. Ke, M. Xu, Y. Wang, M. Yang, K. Du, Z. Fu, D. Kong, D. Dai, Y. Jin, G. Li, H. Li, Q. Peng, J. Wang, W. Huang, *Nature* **2018**, *562*, 249.
[21] K. Lin, J. Xing, L. N. Quan, F. P. G. de Arquer, X. Gong, J. Lu, L. Xie, W. Zhao, D. Zhang, C. Yan, W. Li, X. Liu, Y. Lu, J. Kirman, E. H. Sargent, Q. Xiong, Z. Wei, *Nature* **2018**, *562*, 245.
[22] Y. Wang, X. Li, J. Song, L. Xiao, H. Zeng, H. Sun, *Adv. Mater.* **2015**, *27*, 7101.
[23] Y. Jia, R. A. Kerner, A. J. Grede, B. P. Rand, N. C. Giebink, *Nat. Photonics* **2017**, *11*, 784.
[24] C. Qin, A. S. D. Sandanayaka, C. Zhao, T. Matsushima, D. Zhang, T. Fujihara, C. Adachi, *Nature* **2020**, *585*, 53.
[25] S. Yakunin, M. Sytnyk, D. Kriegner, S. Shrestha, M. Richter, G. J. Matt, H. Azimi, C. J. Brabec, J. Stangl, M. V. Kovalenko, W. Heiss, *Nat. Photonics* **2015**, *9*, 444.
[26] Z. Yang, Y. Deng, X. Zhang, S. Wang, H. Chen, S. Yang, J. Khurgin, N. X. Fang, X. Zhang, R. Ma, *Adv. Mater.* **2018**, *30*, 1704333.
[27] Z. Yang, Q. Xu, X. Wang, J. Lu, H. Wang, F. Li, L. Zhang, G. Hu, C. Pan, *Adv. Mater.* **2018**, *30*, 1802110.
[28] W. Nie, H. Tsai, R. Asadpour, J.-C. Blancon, A. J. Neukirch, G. Gupta, J. J. Crochet, M. Chhowalla, S. Tretiak, M. A. Alam, H.-L. Wang, A. D. Mohite, *Science* **2015**, *347*, 522.

[29] W. S. Yang, J. H. Noh, N. J. Jeon, Y. C. Kim, S. Ryu, J. Seo, S. I. Seok, *Science* **2015**, *348*, 1234.
[30] K. Xiao, R. Lin, Q. Han, Y. Hou, Z. Qin, H. T. Nguyen, J. Wen, M. Wei, V. Yeddu, M. I. Saidaminov, Y. Gao, X. Luo, Y. Wang, H. Gao, C. Zhang, J. Xu, J. Zhu, E. H. Sargent, H. Tan, *Nat. Energy* **2020**, *5*, 870.
[31] F. Li, Z. Yang, M. Jiang, C. Wang, J. Xi, Y. Zhang, C. Pan, J. Lu, R. Wang, *Appl. Phys. Lett.* **2021**, *118*, 071103.
[32] Y. Fu, H. Zhu, A. W. Schrader, D. Liang, Q. Ding, P. Joshi, L. Hwang, X. Y. Zhu, S. Jin, *Nano Lett.* **2016**, *16*, 1000.
[33] Y. Fu, H. Zhu, C. C. Stoumpos, Q. Ding, J. Wang, M. G. Kanatzidis, X. Zhu, S. Jin, *ACS Nano* **2016**, *10*, 7963.
[34] H. Zhu, Y. Fu, F. Meng, X. Wu, Z. Gong, Q. Ding, M. V. Gustafsson, M. T. Trinh, S. Jin, X. Y. Zhu, *Nat. Mater.* **2015**, *14*, 636.
[35] L. Dou, M. Lai, C. S. Kley, Y. Yang, C. G. Bischak, D. Zhang, S. W. Eaton, N. S. Ginsberg, P. Yang, *Proc. Natl. Acad. Sci. USA* **2017**, *114*, 7216.
[36] M. Lai, A. Obliger, D. Lu, C. S. Kley, C. G. Bischak, Q. Kong, T. Lei, L. Dou, N. S. Ginsberg, D. T. Limmer, P. Yang, *Proc. Natl. Acad. Sci. USA* **2018**, *115*, 11929.
[37] B. Tang, Y. Hu, J. Lu, H. Dong, N. Mou, X. Gao, H. Wang, X. Jiang, L. Zhang, *Nano Energy* **2020**, *71*, 104641.
[38] D. Pan, Y. Fu, J. Chen, K. J. Czech, J. C. Wright, S. Jin, *Nano Lett.* **2018**, *18*, 1807.
[39] L. Huang, Q. Gao, L.-D. Sun, H. Dong, S. Shi, T. Cai, Q. Liao, C.-H. Yan, *Adv. Mater.* **2018**, *30*, 1800596.
[40] Z. Yang, T. Albrow-Owen, H. Cui, J. Alexander-Webber, F. Gu, X. Wang, T.-C. Wu, M. Zhuge, C. Williams, P. Wang, A. V. Zayats, W. Cai, L. Dai, S. Hofmann, M. Overend, L. Tong, Q. Yang, Z. Sun, T. Hasan, *Science* **2019**, *365*, 1017.
[41] X. Xu, Z. Han, Y. Zou, J. Li, Y. Gu, D. Hu, Y. He, J. Liu, D. Yu, F. Cao, H. Zeng, *Adv. Mater.* **2022**, *34*, 2108408.
[42] Q. Zhang, R. Su, X. Liu, J. Xing, T. C. Sum, Q. Xiong, *Adv. Funct. Mater.* **2016**, *26*, 6238.